NUCL SCI TECH (2019) 30:142
https://doi.org/10.1007/s41365-019-0667-2

Radiotherapy-customized head immobilization masks: from modeling and analysis to 3D printing

M. A. R. Loja[1,2,3] · D. S. Craveiro[1] · L. Vieira[1,4,5] · E. Sousa[1,4] · J. A. Rodrigues[1] · R. J. F. Portal[1,2]

Received: 1 June 2018 / Revised: 7 May 2019 / Accepted: 14 May 2019 / Published online: 13 August 2019

Abstract Immobilization devices may be a valuable aid to ensure the improved effectiveness of radiotherapy treatments where constraining the movements of specific anatomical segments is crucial. This need is also present in other situations, specifically when the superposition of various medical images is required for fine identification and characterization of some pathologies. Because of their structural characteristics, existing head immobilization systems may be claustrophobic and very uncomfortable for patients, during both the modeling and usage stages. Because of this, it is important to minimize all the discomforts related to the mask to alleviate patients' distress and to simultaneously guarantee and maximize the restraint effectiveness of the mask. In the present work, various head immobilization mask models are proposed based on geometrical information extracted from computerized tomography images and from 3D laser scanning point clouds. These models also consider the corresponding connection to a radiotherapy table, as this connection is easily altered to accommodate various manufacturers' solutions. A set of materials used in the radiotherapy field is considered to allow the assessment of the stiffness and strength of the masks when submitted to typical loadings.

Keywords Computed tomography · 3D laser scanning · Geometric modeling · Head immobilization devices · Stiffness and strength analyses · 3D printing

This work was supported by the Project IPL/2016/SoftImob/ISEL and Project LAETA—UID/EMS/50022/2019.

✉ M. A. R. Loja
amelialoja@dem.isel.ipl.pt

1 CIMOSM, Centro de Investigação em Modelação e Optimização de Sistemas Multifuncionais, ISEL, IPL, Instituto Superior de Engenharia de Lisboa, Av. Conselheiro Emídio Navarro 1, 1959-007 Lisbon, Portugal

2 LAETA, IDMEC, Instituto Superior Técnico, Universidade de Lisboa, Av. Rovisco Pais 1, 1049-001 Lisbon, Portugal

3 Department of Mechanical and Industrial Engineering, Faculty of Science and Technology, NOVA UNIDEMI, Universidade Nova de Lisboa, Caparica, Portugal

4 H&TRC – Health &Technology Research Center, ESTeSL - Escola Superior de Tecnologia da Saúde de Lisboa, Av. D. João II, Lote 4.69.01, 1990-096 Lisbon, Portugal

5 Instituto de Biofísica e Engenharia Biomédica, Faculdade de Ciências da Universidade de Lisboa, Lisbon, Portugal

1 Introduction

Cancer is currently one of the main mortality causes worldwide, making it one of the greatest public health issues. It is estimated that every year 11 million new cases are diagnosed and approximately 7 million people die from cancer. The World Health Organization (WHO) considers that it will be the principal cause of death by the year 2020 [1]. Thus, as radiotherapy is an important treatment modality for patients with various types of tumors, there is a need for immobilization systems to provide an effective degree of rigidity, together with an acceptable degree of comfort for the patient. However, no matter which mask molding process is considered, it can be particularly distressing for patients and even intolerable for those who suffer from claustrophobia. Although the full-head mask can be cut open around the eyes and mouth to improve patients' comfort, mask cutting after molding is difficult, producing sharp edges. Moreover, when a thermoplastic mask is produced, different parts of it are stretched by different amounts, changing its size and thickness. In the context of diagnosis or preliminary planning, a typical positron emission tomography (PET) brain imaging session can last up to half an hour, and it is not reasonable to expect a patient to remain motionless during this period. There are no standard or routine screening tests for head and neck cancers. Standard treatments for head and neck cancers include radiation therapy and surgery, and for certain types of head and neck cancer, chemotherapy [2, 3]. Radiation therapy aims to deliver an appropriate tumoricidal dose while respecting the radiation tolerance of adjacent tissues, so it is also important to consider that the application of radiotherapy is often constrained by sequelae to the surrounding tissue outside the treatment field.

The use of head restraints is thus crucial [4, 5], despite the reported discomfort and/or claustrophobia they may produce.

The evolution of reverse engineering techniques has contributed to the development of new interdisciplinary research areas, specifically those involving medicine and engineering areas, with effective benefits for patients and various scientific areas. It is in this interdisciplinary context that it is important to find useful solutions to this problem.

A review of the literature suggests that a combination of acquisition and reconstruction techniques, as well as subsequent modeling, can provide purpose-oriented customized devices. Immobilization devices for limbs [6] and other body areas can promote a better constraint of the anatomic segments for increased diagnosis success and image quality. In fact, currently used restraint devices have been revealed to be inaccurate for keeping the patient in the correct position, compromising the effectiveness of the medical procedure [7]. Only a few published works are found in this multidisciplinary context. Concerning head immobilization systems, there have been only a few studies; these include recent reports by Fisher et al. [8] and Chen et al. [9]. Fisher et al. [8] performed a preclinical evaluation of an immobilization system for patients undergoing external beam radiation treatment of head and neck tumors. The mask only modeled a phantom face, and it was manufactured from a 3D model, built using the computed tomography (CT) data routinely acquired for treatment planning. The mask was composed of a continuous 4-mm-thick surface without holes, with no additional surfaces or fixation devices to connect to a radiotherapy table. The authors used the Hausdorff distance to analyze CT slices obtained by rescanning the phantom with a printed mask in position. The authors concluded that for more than 80% of the slices, the median "worse-case" tolerance is approximately 4 mm; thus, the analyzed mask was able to achieve similar levels of immobilization as those of current systems. Chen et al. [9] proposed an automatic framework to construct and produce immobilization masks for radiation therapy of the head/-neck. These authors used 3D printing technology along with image analysis approaches based on 3D CT image data. As in the study by Fisher et al., these authors only considered construction of the facial model, discarding any connection to an "exterior" table and the necessary correspondence between these parts of the system as a whole. The model construction considered the extraction of the skin surface of the head/neck/shoulder, after which the facial features were recognized automatically based on deformable shape models. The 3D model obtained was an open shell with holes in the eyes, nose, and mouth locations. In this case, no assessment of the effectiveness of such a model was performed.

More recently, Sousa et al. [10] considered the possibility of obtaining the geometrical characteristics of a phantom head (PIXI) skin surface using various acquisition sources, namely 3D laser scanning (3DLS) and computed tomography. From the statistical analysis they performed, they concluded that there were no significant statistically differences when measuring the anthropometry features based on the different 3D full-head models obtained.

To the author's knowledge, there are no published works that consider the global process, starting at data acquisition and proceeding to analysis and production of a complete head immobilization system.

To enable this, the present work is organized in three main stages. In the first stage, related to the acquisition of the head geometry and the customized design of the corresponding masks to fit the head computational models, the necessary data were acquired via CT and 3DLS. These data were subsequently processed to reconstruct the corresponding 3D surface models. The masks' full models (with no holes) were primarily developed taking into account three aspects: the obtained head surfaces, a head support commonly used in clinical practice, and the required connection to a radiotherapy table.

In the second stage, taking into account some patients' informal opinion related to the aspects that would be of help to minimize the claustrophobia sensation, three different geometries were designed by removing material from the full masks. The possibility of making these masks from different materials used in the radiotherapy field was considered to proceed to analysis concerning the immobilization effectiveness and material strength.

The final stage of the present work involved in the production of the immobilization masks via fusion deposition modeling (FDM) 3D printing of these models and characterization of the production parameters for the various designed masks, to enable a future assessment in terms of costs.

This complete procedure framework to obtain immobilization masks for the head and eventually also for the neck is foreseen to have an effective application not only in radiotherapy, but also in brain imaging.

2 Materials and methods

The main objective of the present work is the establishment of a data flow from the geometry acquisition of the head 3D surface to production of the corresponding immobilization mask. To this purpose, the head of a physical phantom (PIXI) used in radiotherapy and nuclear medicine for teaching purposes was used. To achieve this purpose, two data sources were considered: computed tomography (CT) images and the point clouds originated via 3D laser scanning (3DLS). The details concerning the equipment and acquisition conditions will be mentioned in Sect. 2.1.

It is important to note here that the reason why these two approaches are considered is related in the first case to the fact that CT is a diagnosis/planning tool that may also be used to obtain the customized mask, thus eliminating the usual manual conformation to the head. The use of 3DLS is considered because it is a noninvasive technique used in other science fields; thus, it can be used as an alternative to CT because according to the conclusions obtained in a previous work by some of the co-authors, no statistically significant differences are observed between the models achieved using different approaches [10, 11].

According to the logical procedure flow that structures the present work, Sect. 2.2 describes various aspects that guided the design of the geometrical modeling of the different mask geometries, as well as their connection to the radiotherapy table. The requirements that the materials of the masks have to meet are the object of Sect. 2.3, taking into account the radiotransparency by considering different materials that according to the manufacturers may offer potential solutions, and the mechanical/physical properties that will be needed to fulfill both production and immobilization purposes, without mechanical failure.

The definition of the loads to which the masks will be submitted is addressed in Sect. 2.4 to assess the masks' performance and thus provide better/feasible solutions. As this information is not found in the literature, the conclusions of a study in another field of science, which analyzed the maximum forces developed when athletes perform a different set of movements, were utilized. Finally, Sect. 2.5 characterizes the conditions and parameters of the FDM 3D printing considered for mask production via FDM 3D printing.

2.1 Phantom head geometrical models

In this study, a 3D Scanner Ultra HD from NextEngine was used to acquire the 3D point cloud of the phantom head, and a PET/CT, model Gemini TF 16 (Philips Healthcare, Netherlands, Europe), was used to obtain the CT images. The point clouds were obtained considering a medium range acquisition and a number of ten sectors (36° angles) with a density of 132 points per cm^2. The CT was performed using the settings often used in a normal planning CT: 1 mm slice thickness, 20 mAs, 120 kVp, pitch of 0.938, 512 $\times$ 512 pixel matrix, and rotation speed of 0.5 s per rotation.

The CT images were next used to reconstruct the 3D head surface, using the 3D Viewer plug-in of ImageJ [12], whereas the global point cloud was obtained at the end of the scanning process. In both cases, the surface obtained from ImageJ and the point cloud obtained from the 3D Scanner Ultra HD software (NextEngine ScanStudio) were imported to the computer-aided design application SolidWorks [13] to further obtain a polygonal mesh for subsequent elimination of eventual defects, e.g., holes. The models were next converted to solid entities to proceed to the mask modeling stage.

Figure 1a illustrates the PIXI head during the 3DLS acquisition, Fig. 1b presents the corresponding solid model obtained from 3DLS, and Fig. 1c shows the solid model obtained from CT (1-mm slice thickness).

The 3DLS reconstruction is more detailed, which is explained by the high definition of the scanning system used. However, as some of the present co-authors concluded in a preliminary study [10], there are no statistically significant differences in the measurements of a set of head anthropometric features using the different 3D full-head models obtained. Additionally, these regions with different levels of detail will be eliminated in the designed masks as they coincide with the introduced "holes."

2.2 Immobilization mask models

Based on the two head models obtained and taking into account the main characteristics of head supports that can be found on various manufacturers' websites, the next step was modeling of such an auxiliary device adapted to the PIXY head. This device model was also designed using SolidWorks, and its elevator and support functions are illustrated in Fig. 2. At this stage, a set of possible design configurations was considered, bearing in mind the comfort of the patient and minimization of claustrophobia.

With the head supported and in position, a full surrounding surface was extruded toward the radiotherapy table plane, where it meets a U-shaped fixture though which the connections to the table will be made. The

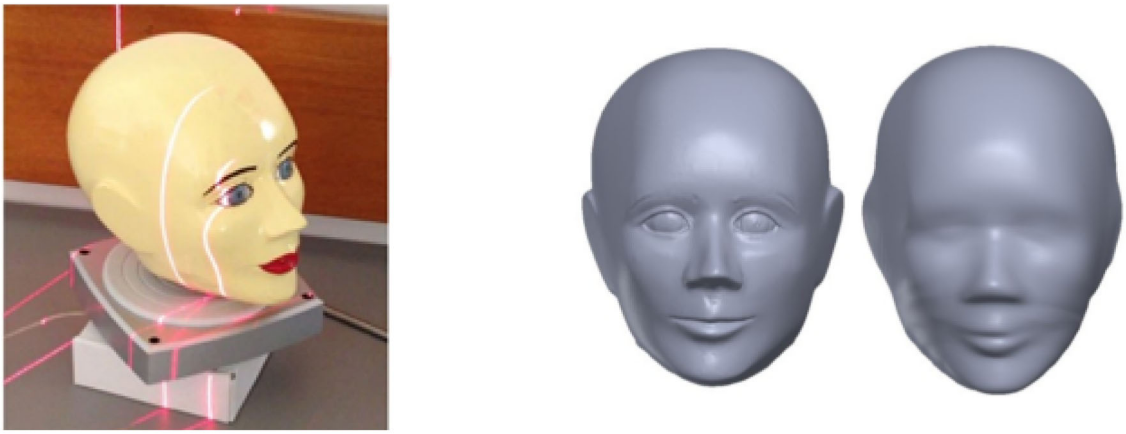

Fig. 1 **a** 3D laser scanning (3DLS) of PIXI head, **b** 3DLS head model, and **c** CT head model (color online)

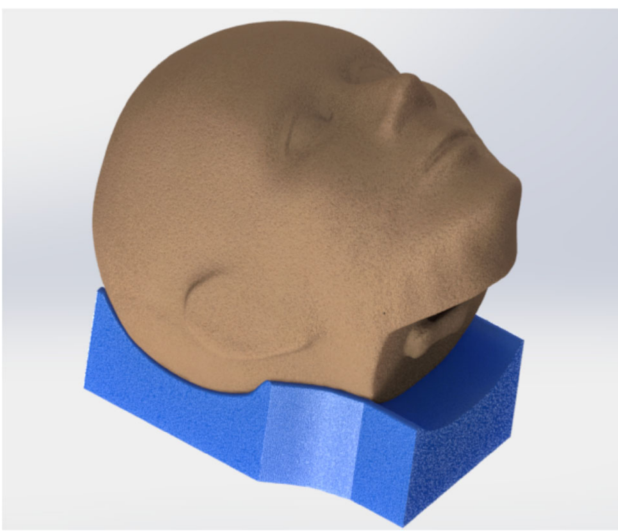

Fig. 2 Fitting 3D head model in adapted support model

fixture and the immobilization mask were bonded horizontally (table plane). This process was performed for both the 3DLS and CT head models (Fig. 3).

Three geometric configurations were next designed for both the 3DLS and CT immobilization masks, as presented in Fig. 4.

To simplify the reference to the various mask models (Fig. 4), the following nomenclature was adopted: M* denotes the model (M) geometry and the symbol (*) may assume the values 1–3 (three geometric configurations). The following designations (CT or 3DLS) have already been defined in this document and are related to the data acquisition method.

As it is possible to observe, these masks' configurations differ from the ones presently used, as they are much less closed, thus providing a less stressful treatment. The designed geometries were based on the opinion of some patients about the areas that they would think would alleviate the discomfort of the mask. However, other geometry solutions may naturally be considered and analyzed. It is fundamentally worth mentioning that as these masks will not be manually molded to the patient's head as currently occurs, they will not be affected by variations in their

Fig. 3 CT (left) and 3DLS (right) full masks before final design configurations

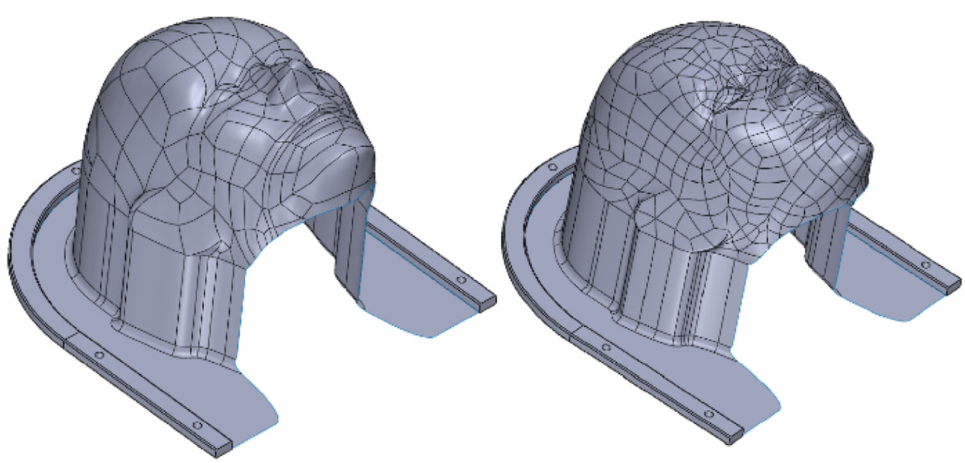

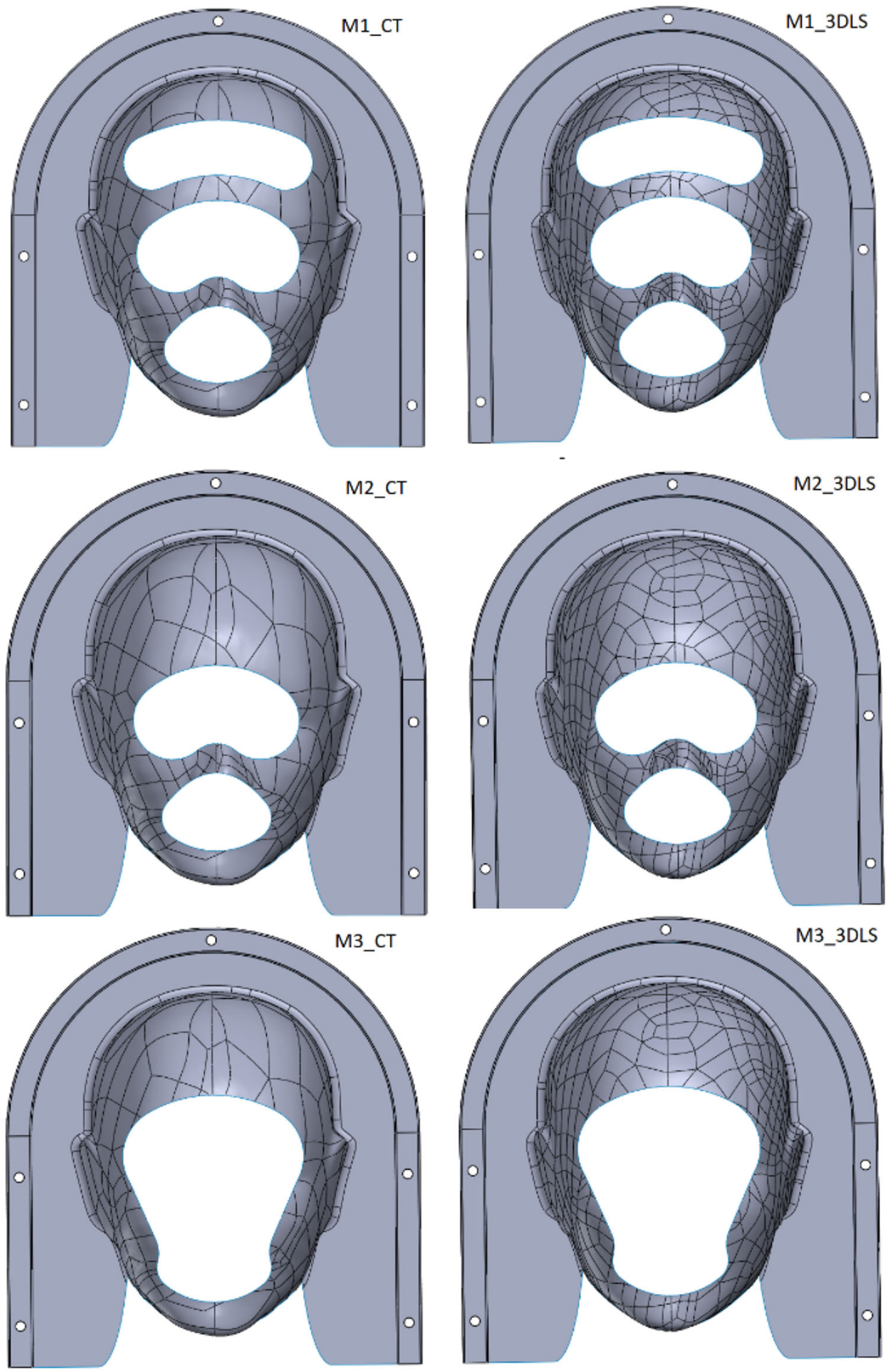

Fig. 4 Various immobilization mask geometries

thickness and hole distortions, which is another drawback of actual systems.

Another characteristic of these masks is that by default they are fully conformed to the head surface model. The existence of any clearance, restricting only some anatomical points, may be considered if found adequate, but in the present work, a total contact surface to the head solid model was considered.

2.3 Masks' material properties

As these masks are intended to be manufactured using an additive technique, namely fusion deposition modeling 3D printing, the selection of materials for these devices is dependent on the minimum extrusion temperature suitable for 3D printing manufacturing, and of course because of the operation conditions of the masks, on the mass attenuation coefficient.

From the materials' databases and technical datasheets available [14, 15], four materials were selected that would be able to meet both the operating conditions and the production requirements, namely polymethyl methacrylate (PMMA), polyphenylene sulfide, polycarbonate, and acrylonitrile butadiene styrene (ABS), which are denoted hereafter as T1, T2, T3, and T4, respectively.

The mean values of the material properties with relevance for the present work are presented in Table 1.

It is relevant to note that any other material may be easily considered for simulation purposes; however, it should observe the previously mentioned requirements.

2.4 Masks' mechanical performance

Considering the immobilization objective of these masks, it is fundamental to guarantee that they will accomplish the required performance from a mechanical perspective. Accordingly, an analysis of the static behavior of the masks when submitted to typical loading situations was carried out using the finite-element method [16, 17]. To simulate the connection of the masks to the table, the degrees of freedom associated with the fixture holes were constrained.

The selection of the loads to apply was based on a study by Almosnino et al. [18], which focused on the force-generating capacity of neck muscles under isometric conditions by athletes. Considering this, and the probable patient's movement intention, two case studies were analyzed. The first case simulates a left lateral bending of the neck with 158.1 N applied on the left side of the mask (Fig. 5a).

The second study considers a flexion of the neck with 152 N applied on the front of the mask (Fig. 5b). The corresponding computational modeling of these loads can be observed in the free body diagram of 3DLS masks in Fig. 6-top for the lateral bending load of the neck. Similar diagrams were also obtained for CT masks.

To better approximate the actions associated with each movement translating the forehead surface ability to support higher loads when compared with other regions of the face, these load actions were modeled as linearly varying loads.

Similarly, Fig. 6-bottom illustrates the load corresponding to the neck flexion movement, through a free body diagram, where the forces corresponding to the boundary conditions at the points where the masks are fixed to the table are also visible.

Table 1 Material properties [14, 15]

Properties	Material ID			
	T1	T2	T3	T4
Young's modulus, E (GPa)	3.30	4.33	2.36	2.10
Poisson's ratio, ν	0.43	0.40	0.33	0.35
Yield strength, σ_{ys} (MPa)	86.00	154.50	63.30	40.70
Melting point (°C)	218	282	302	221
Molding point (°C)	64.50	135.00	84.50	59.70
Density, ρ (g/cm^3)	1.19	1.37	1.20	1.05
Tolerance level to radiation, KGY	100	1000	1000	1000

2.5 3D printing mask models

To illustrate the final stage of the present work, three mask configurations were manufactured in a Makerbot Replicator 3D printer (Makerbot). Considering that at this stage, the masks manufacturing has a single illustration purpose, the three mask models were printed in a 1:2 scale. The three mask models were printed using a 15% hexagonal infill scheme, which corresponded to an estimated printing time of 4 h 47 min, 4 h 46 min, and 4 h 08 min, respectively, for models M1, M2, and M3. The estimated masses for each model were 94.36 g, 95.74 g, and 83.56 g, respectively, for both 3DLS and CT models, as will be mentioned in the next section.

3 Results and discussion

In this section, first, the convergence studies developed for the masks are presented. Next, the characterization of the influence of the thickness on these masks, made from the materials listed in Sect. 2.3, is presented. For various typical head movements, a finer-tuning analysis is performed concerning the relationship between the desired immobilization degree and the mask thickness.

3.1 Convergence analysis

For the convergence analysis, the masks are made of T1 material (PMMA) and submitted to a left lateral bending load. The thickness of the mask was set at 4 mm. The convergence study was performed according to an h-refinement approach, i.e., by increasing the number of

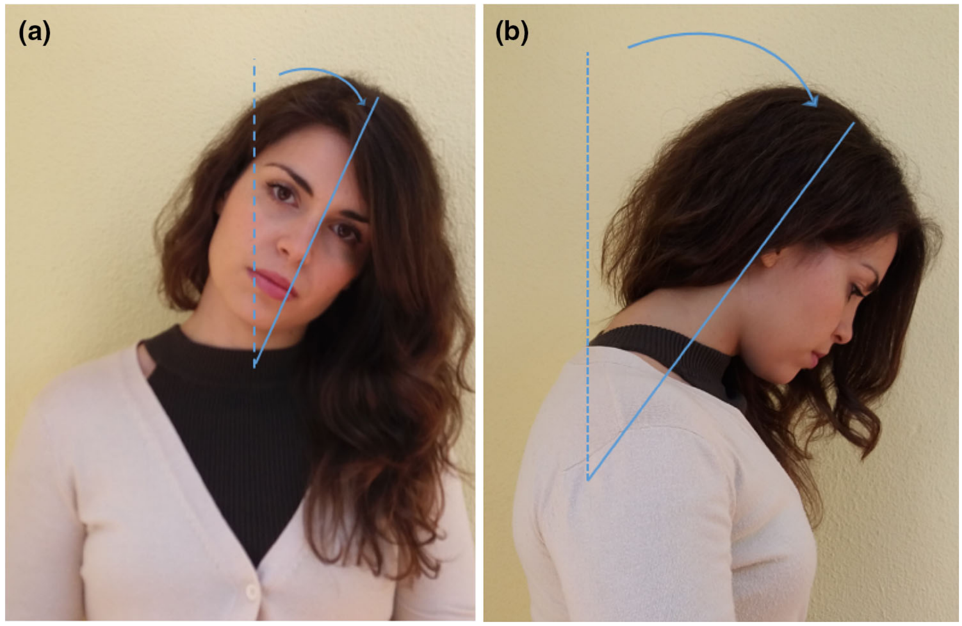

Fig. 5 **a** Neck lateral bending and **b** neck flexion

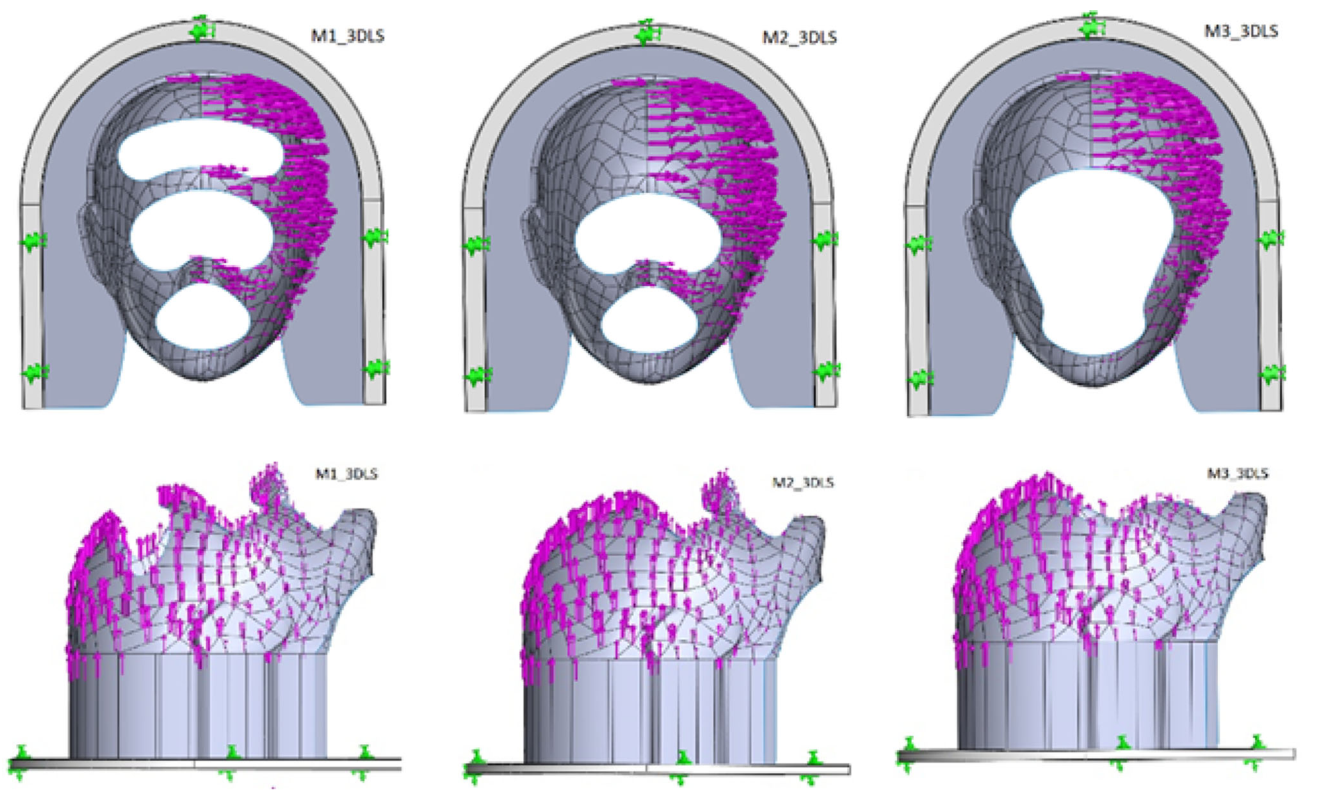

Fig. 6 (Top) Free body diagrams for three 3DLS models under left lateral bending load. (Bottom) Free body diagrams for three 3DLS models under flexion load (color online)

elements, thus reducing the characteristic dimensions. The analyzed quantities considered relevant for this study were the equivalent von Mises stress and the resultant displacement, to, respectively, ensure that the maximum equivalent stress will be less than the material yield stress and that the maximum displacement will also be consistent with the desired immobilization. Figure 7 presents the convergence results for the resulting maximum displacement for all mask models.

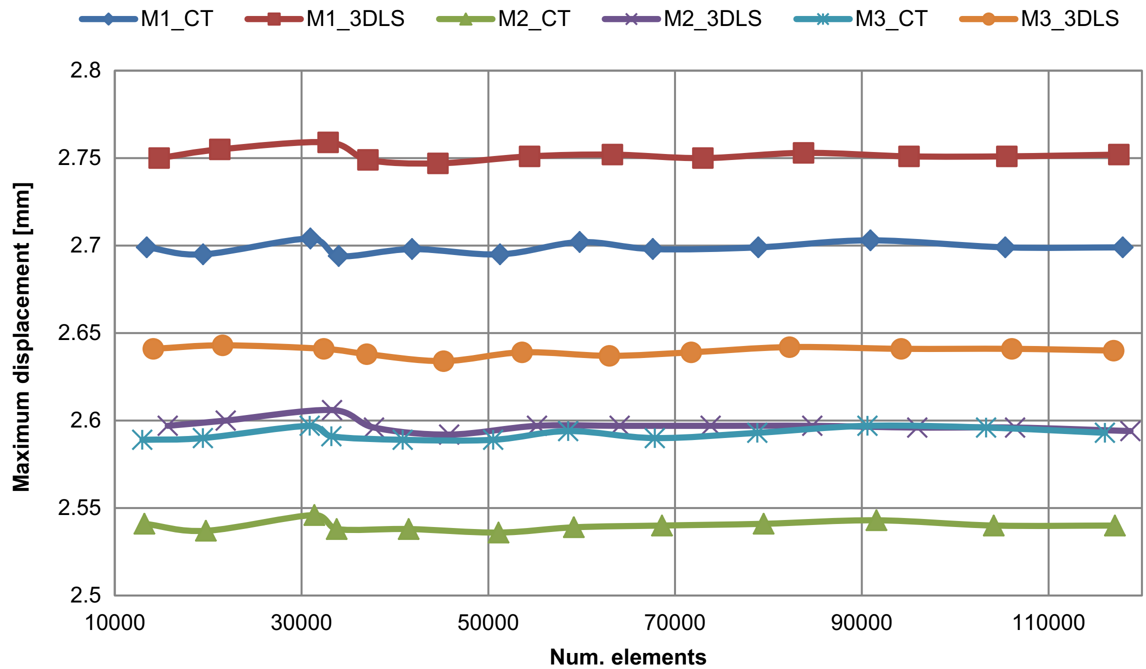

Fig. 7 Maximum resulting displacement for CT and 3DLS mask models (mm) (color online)

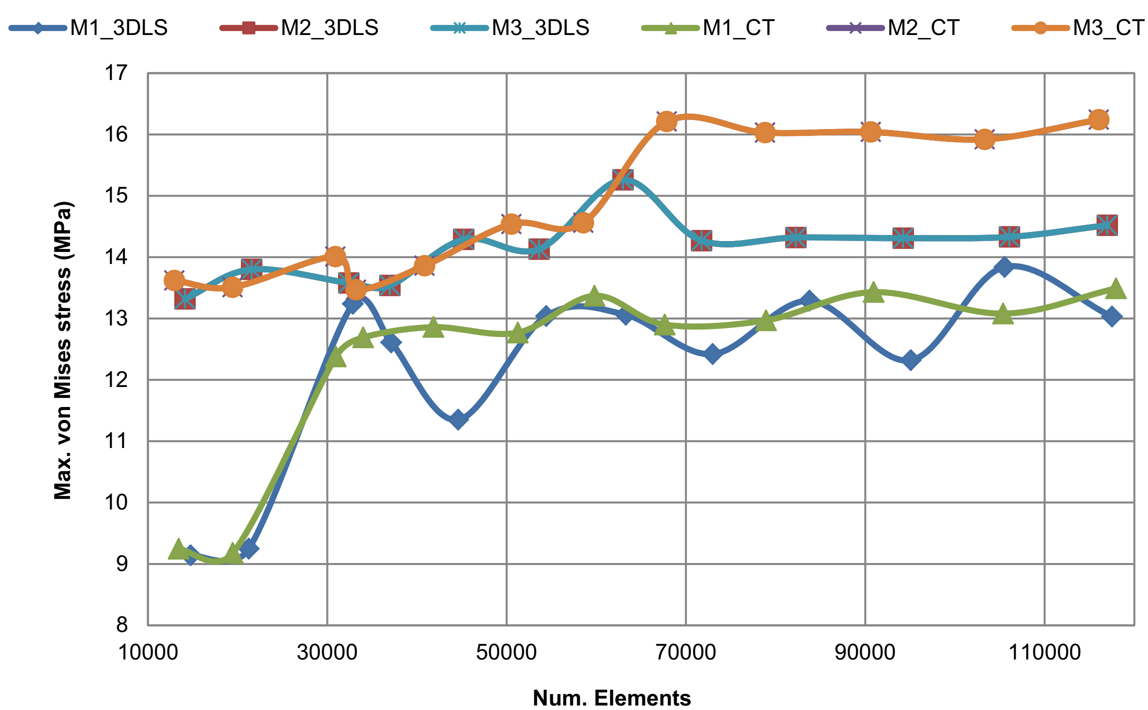

Fig. 8 Maximum von Mises stress for CT and 3DLS models (color online)

Figure 8 shows the curves depicting the von Mises stress as a function of the number of elements associated with the h-refinement.

From Figs. 7 and 8, it is possible to see that, with the exception of the 3DLS, all the models present a globally convergent pattern. Nevertheless, this model presents an oscillatory behavior around a mean value that will likely disappear with more refined meshes. Concerning the maximum displacement, it is possible to see that in the M1 configuration there is a slight difference between the values obtained with the models reconstructed from the CT images and those from the point cloud. In the context of the equivalent stress, we also observe a slight oscillation, although with a convergent trend. Configurations M2 and M3 and their corresponding 3DLS and CT models present a similar convergence behavior for both the displacements and the von Mises stress. It is relevant to note that, in all cases, the maximum equivalent stress is far lower than the yield point (86 MPa), providing a high safety factor.

To complement these results, Fig. 9 presents, for the three geometries and one of the acquisition methods (CT), the distributions of both the von Mises stress and displacement, using the last finite-element mesh of the convergence studies.

It is important to add that the 3DLS models present similar results to those shown in Fig. 9, concerning both

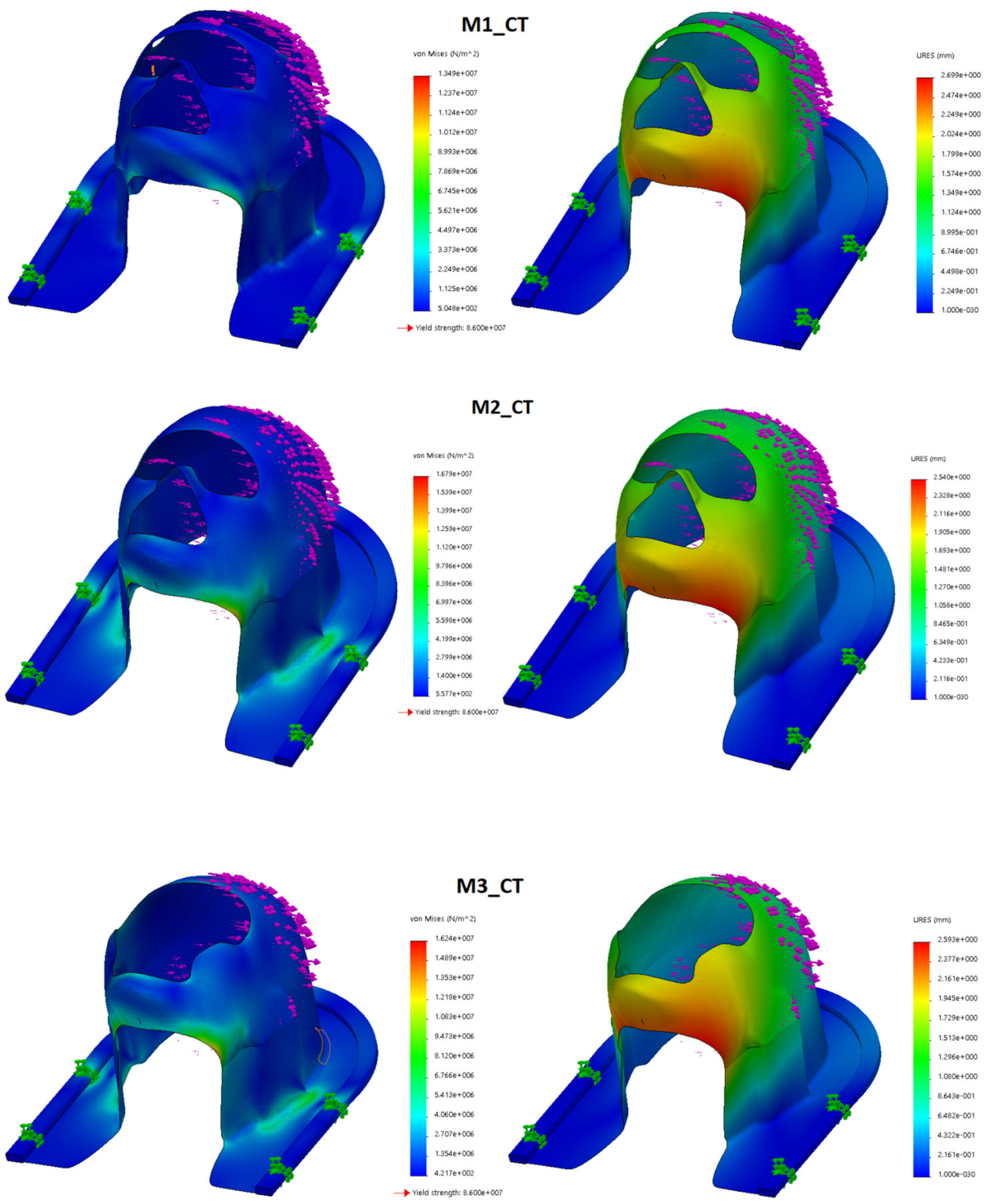

Fig. 9 Maximum von Mises stress and resulting displacement for M1_CT, M2_CT, and M3_CT models (color online)

the distributions and maximum values of the resultant displacement and von Mises stress.

3.2 Influence of material and thickness

In addition to the previous static convergence analysis, where only a material and a constant thickness were applied, a new study was developed.

Considering four different thicknesses and four different materials, the static analysis was rebuilt with the last mesh obtained in the convergence study for all masks.

3.2.1 Maximum displacement

The results obtained for the same neck lateral bending load are presented in Table 2, for all the masks, considering a discrete set of thickness values ranging from 3 to 5 mm.

There is an expected inverse relationship between the mask thickness and the maximum displacement. The material that performs best, according to the immobilization objective, is T2.

Concerning the geometry, the M2 model presents the lowest values of displacement, closely followed by the M3 model. This allows an additional conclusion: the masks with forehead constraint perform better than those without it.

3.2.2 Mask safety factor

The safety factor associated with the strength of each of the designed immobilization devices is an important aspect to consider. Therefore, the safety factor was also evaluated for the previous thicknesses and materials. The results obtained are presented in Table 3.

From these results, it is possible to conclude that the material T2 yields the highest safety factors. Concerning the geometric configurations of the masks, it is also clear that M2 is responsible for the greatest values. It is also possible to conclude that the masks made with the T2 material present the best safety factors. This is verified for all the geometric models. On the contrary, the material that demonstrates the worst performance from the safety factor perspective is T4.

Considering the results listed in both tables, it can be globally concluded that despite a 5-mm thickness, high safety factors are achieved, and this most likely would not be necessary, as the selected degree of immobilization requires that thicker masks be used. Therefore, the stiffness constraint prevails over the strength constraint.

To enable a better illustration of the factor evolution trend, Fig. 10 depicts the influence that the mask thickness has on the safety factor for the M2 configuration with each material and both 3DLS and CT models.

Regarding the relationship between the safety factor and the mask thickness, it is also possible to conclude that the former increases as the thickness increases. As this safety factor has a relationship between the material yield strength and the maximum von Mises stress, the visible trend

Table 2 Maximum resulting displacement (mm)

Thickness (mm)	Mask model					
	M1_CT	M2_CT	M3_CT	M1_3DLS	M2_3DLS	M3_3DLS
T1 (polymethyl methacrylate)						
3	5.575	5.214	5.326	5.707	5.347	5.444
4	2.699	2.540	2.593	2.752	2.594	2.640
5	1.528	1.443	1.472	1.555	1.471	1.495
T2 (polyphenylene sulfide)						
3	4.242	3.969	4.053	4.343	4.071	4.144
4	2.055	1.934	1.975	2.095	1.976	2.011
5	1.164	1.100	1.121	1.185	1.121	1.139
T3 (polycarbonate)						
3	7.728	7.235	7.386	7.916	7.424	7.555
4	3.748	3.530	3.603	3.823	3.608	3.670
5	2.127	2.011	2.049	2.164	2.050	2.082
T4 (acrylonitrile butadiene styrene)						
3	8.707	8.150	8.321	8.917	8.362	8.510
4	4.221	3.975	4.057	4.306	4.062	4.132
5	2.394	2.263	2.306	2.436	2.307	2.343

Table 3 Maximum mask safety factors

Thickness (mm)	Mask model					
	M1_CT	M2_CT	M3_CT	M1_3DLS	M2_3DLS	M3_3DLS
T1 (polymethyl methacrylate)						
3	2.8	3	3.1	3.3	3.5	3.5
4	4.8	5.1	5	5.6	6	4.7
5	6.9	7.1	5.6	7.3	6.9	5.3
T2 (polyphenylene sulfide)						
3	4.1	4.4	4.4	4.7	5	5
4	6.9	7.4	7	8	8.5	6.7
5	9.7	9.9	7.9	10	9.6	7.6
T3 (polycarbonate)						
3	2.2	2.4	2.3	2.5	2.6	2.6
4	3.8	4	3.6	4.2	4.3	3.5
5	4.8	4.9	4.1	5.1	4.8	3.9
T4 (acrylonitrile butadiene styrene)						
3	1.4	1.5	1.5	1.6	1.7	1.7
4	2.4	2.6	2.3	2.7	2.8	2.2
5	3.1	3.2	2.6	3.3	3.1	2.5

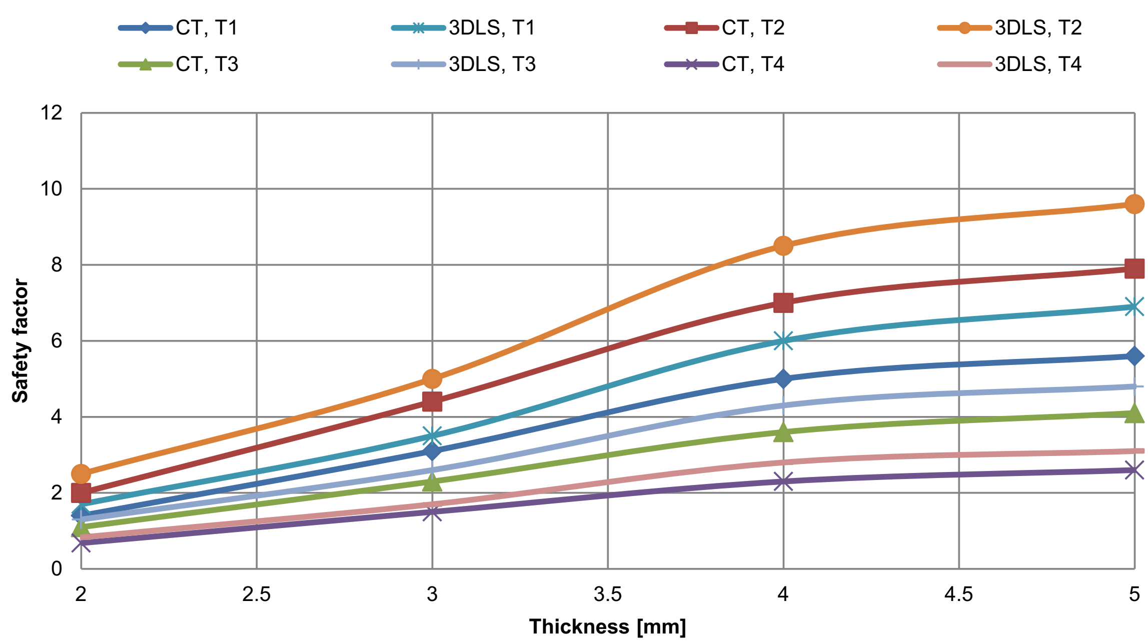

Fig. 10 Safety factor as a function of mask thickness for different materials, for M2 configuration (color online)

evolution means that this stress decreases as the mask thickness increases. Although there are slight differences between the safety factors associated with each mask geometry when the data source is the 3DLS or the CT, this is not relevant because even in the most unfavorable case, the yield strength of the material is not attained, i.e., the maximum equivalent stress stays below that value. Thus, the structural integrity of the mask would not be compromised.

3.3 Stiffness criterion assessment

As it is possible to conclude from the previous results, the maximum displacement always occurs in the lower jaw region for all the models considered. This is a localized phenomenon associated with the fact that this region has a larger free edge. However, it is also clear that the remaining regions of the mask present stiffer behavior. Although the stiffening of this region can be achieved through local mask thickening, this could contribute to a differentiated behavior concerning the attenuation, so to improve the stiffness performance of the masks, a finer-tuning analysis was developed considering a maximum displacement of 1 mm as an acceptable value.

Considering that the material that performed best in previous studies was T2, it was selected for the present case study. The analyzed loading cases were the two mentioned above, corresponding to neck lateral bending and neck flexion (Fig. 5). An iterative procedure was adopted that utilized a 0.1-mm increment, which would be comparable with the resolution of 3D printers. The results obtained are presented in Tables 4 and 5.

In a lateral bending load situation, all the models present similar results. However, the M1 masks require a slightly higher thickness value to provide a displacement less than 1 mm. The M2 models present a good behavior, followed by the M3 ones. Although constituting a slightly less severe load case, the flexion of the neck is probably a more natural movement; thus, it is important to analyze the effects the corresponding load would produce in the immobilization masks.

Concerning the results achieved for the neck flexion load, the M2 masks require a slightly lower thickness to achieve maximum displacements below the established 1-mm limit. Again, one may conclude that the masks that restrain the forehead present better performance. Figures 11 and 12 illustrate the maximum resultant displacement for the M2_CT model when submitted to each of the load cases.

From Figs. 11 and 12, it is possible to have a global view of the distribution of the resultant displacements for the entire mask. When the load case corresponds to neck flexion, as presented in Fig. 11, the resultant displacements are highest at the chin region and nose.

A similar situation occurs for the lateral bending load, where the highest displacement values occur at the lower jaw region.

This occurs in both cases, which is expected, as one has larger free edges. Nevertheless, it is also worth noting that for the other mask regions, the resultant displacement clearly decreases.

Concerning the von Mises distributions associated with the same mask under the two load cases, Figs. 13 and 14 clearly illustrate that their maximum values are far from the material yield stress.

3.4 3D printed masks

As mentioned above, the masks were printed using a reduced 1:2 scale, as the purpose in the present context was illustrative. The physical models obtained can be observed in Fig. 15.

A study of the effects that different infill characteristics and percentages have on the estimated normalized printing time and filament mass was conducted.

Table 6 presents the non-dimensional masses m and printing times Δt required for the three models for different hexagonal and linear infill percentages. This normalization was carried out considering the ratio between each value and the corresponding solid version value.

It is possible to conclude there is not a linear relationship between the infill percentage and the estimated time and mass. This is not only because of the characteristics of each mask, but also because of the different needs concerning the printing supports, which is a requirement of the 3D printing technique used.

Although the results presented in Table 6 are related to those obtained for the 3DLS masks, it is relevant to note that the printing times and masses are similar for CT masks. In fact, the masks are quite similar, as the regions where they differ in detail when considering the full masks (no holes) were removed to achieve the various hole geometries.

The results obtained suggest the viability of establishing an automated manufacturing procedure for head immobilization masks. Based on the present conclusions, it is necessary for another study to be carried out to assess/quantify the influence of such an automated solution on the minimization of some sources of patients' distress, although this is an expected result.

It is also important to state that although such different procedures may imply changes in clinical protocols, this may pave the way for improved conditions and therefore perspectives for the diagnosis and therapeutic of brain diseases. However, following the present work, other

Table 4 Maximum displacement obtained for CT and 3DLS masks: left lateral bending

Thickness (mm)	Maximum displacement (mm)					
	M1_CT	M1_3DLS	M2_CT	M2_3DLS	M3_CT	M3_3DLS
5	1.164	1.185	1.100	1.121	1.121	1.139
5.1	1.107	1.126	1.046	1.066	1.066	1.083
5.2	1.053	1.071	0.996	1.015	1.015	1.030
5.3	1.003	1.021	–	0.967	0.967	0.982
5.4	0.957	0.973	–	–	–	–

Table 5 Maximum displacement obtained for CT and 3DLS masks: flexion

Thickness (mm)	Maximum displacement (mm)					
	M1_CT	M1_3DLS	M2_CT	M2_3DLS	M3_CT	M3_3DLS
2	2.050	2.120	1.858	1.925	2.071	2.128
2.1	1.809	1.869	1.639	1.697	1.824	1.874
2.2	1.607	1.660	1.456	1.507	1.618	1.661
2.3	1.436	1.483	1.301	1.346	1.444	1.482
2.4	1.291	1.334	1.170	1.210	1.296	1.330
2.5	1.167	1.206	1.058	1.094	1.170	1.200
2.6	1.060	1.096	0.961	0.993	1.061	1.088
2.7	0.968	1.000	–	–	0.966	0.991

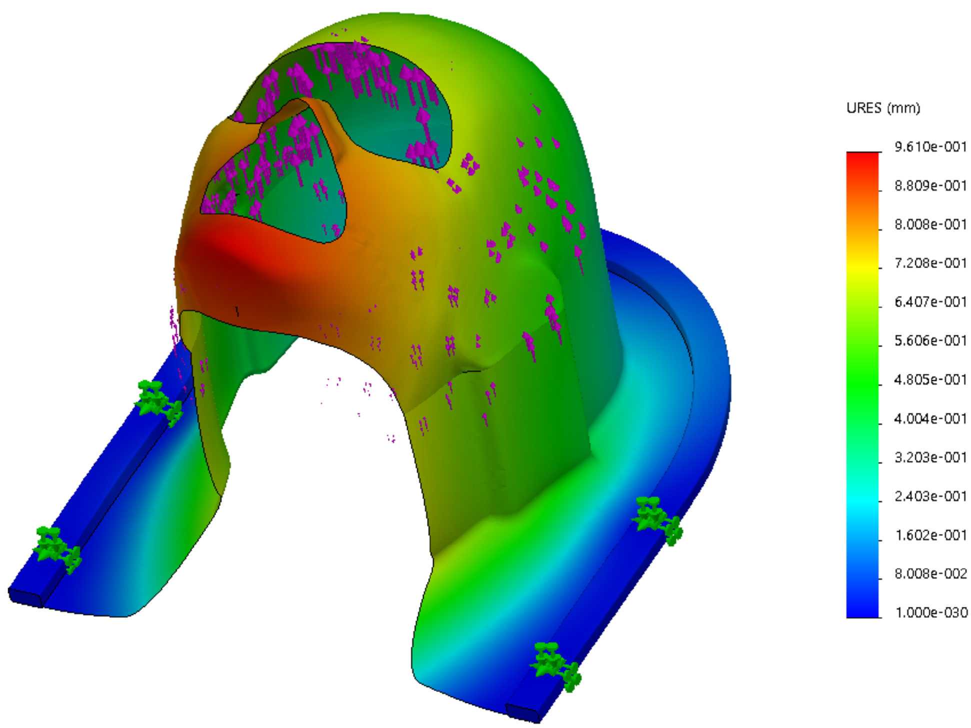

Fig. 11 Maximum resultant displacement, for M2_CT model. Neck flexion load case (color online)

studies concerning radiation attenuation will be required to determine the most suitable material for this purpose.

4 Conclusion

Immobilization medical devices may be a valuable aid to ensure improved effectiveness for specific therapies. The objective of the present study was to present a preliminary design of various head immobilizations masks considering the anthropometric characteristics acquired via computed tomography and 3D laser scanning.

From the analyses developed, it was possible to conclude that there were no remarkable differences regarding the responses provided by the same mask configuration, regardless of the head geometry acquisition source. Therefore, it is possible to consider alternative methods of acquiring external anatomic parts, thus minimizing the exposure of the patient to high-energy radiation.

Considering the results obtained for the proposed mask configurations, it can be concluded that the immobilization requisite is the criterion that most affects the thickness. The strength criteria illustrated via the von Mises maximum stresses denote that, in any situation, these stresses are far lower than the material yield stress point, thus ensuring a high strength safety factor.

These results suggest the feasibility of a complete computational design and manufacturing procedure to achieve head immobilization systems. It is also possible to state that the established methodology can be used for other regions of the body, for different immobilization conditions, allowing for eventual localized clearances.

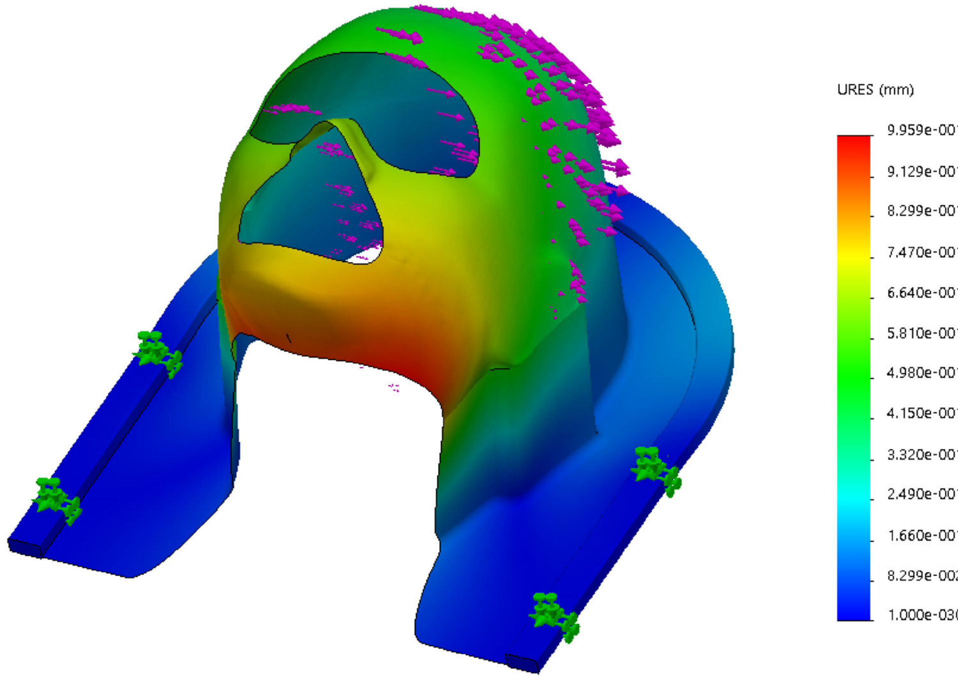

Fig. 12 Maximum resultant displacement for M2_CT model. Neck lateral bending load case (color online)

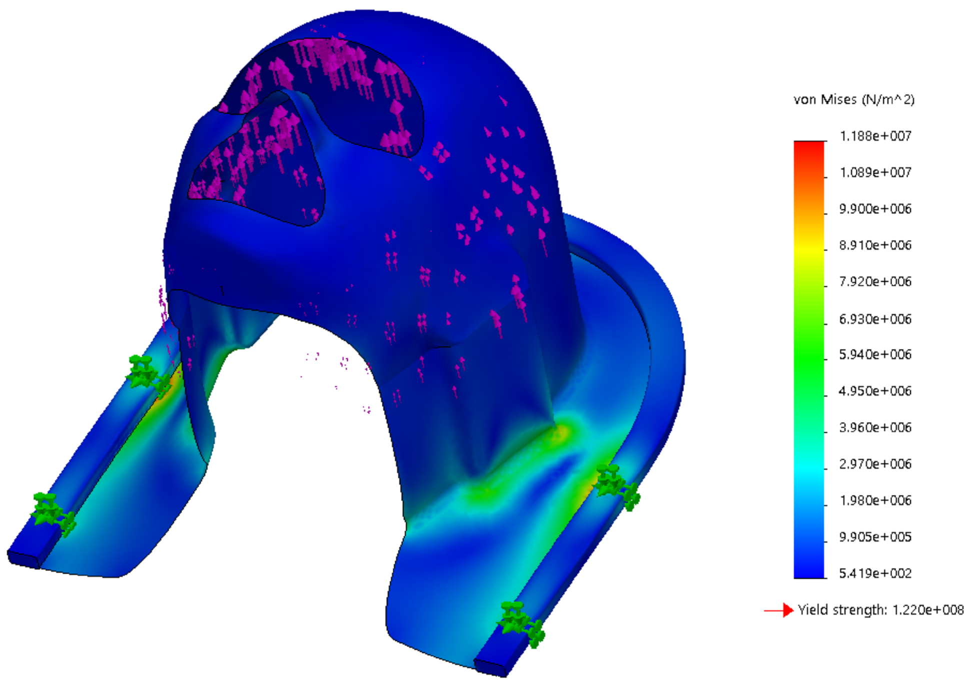

Fig. 13 von Mises stress distribution for M2_CT model. Neck flexion load case (color online)

Although the mechanical performance of the different masks has been successfully tested for a set of movements, other movements may be considered, if they are found to be important to characterize situations that may occur during the real conditions associated with radiotherapy treatment. However, this will require an accurate previous estimation of the load the patient will exert when performing a specific movement.

Further studies are still necessary to evaluate the physical properties of the 3D printed masks when in contact with radiation. It is also necessary to take into account limitations such as the printing time and the economic costs of the masks to evaluate whether they can be a feasible alternative to those available in current clinical practice. Additionally, and based on these conclusions, it will be important to determine what improvements and/or

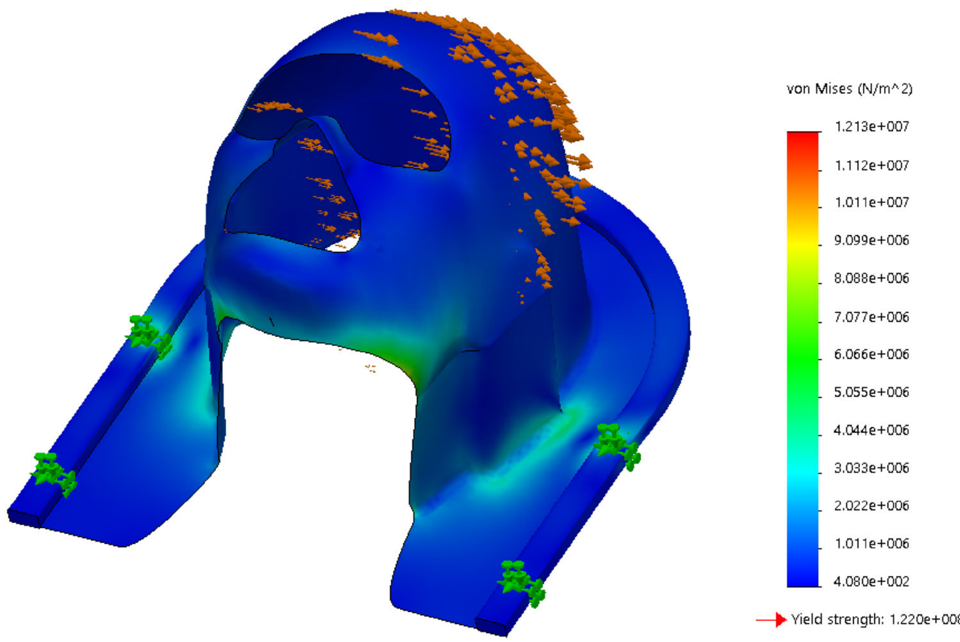

Fig. 14 von Mises stress distribution for M2_CT model. Neck lateral bending load case (color online)

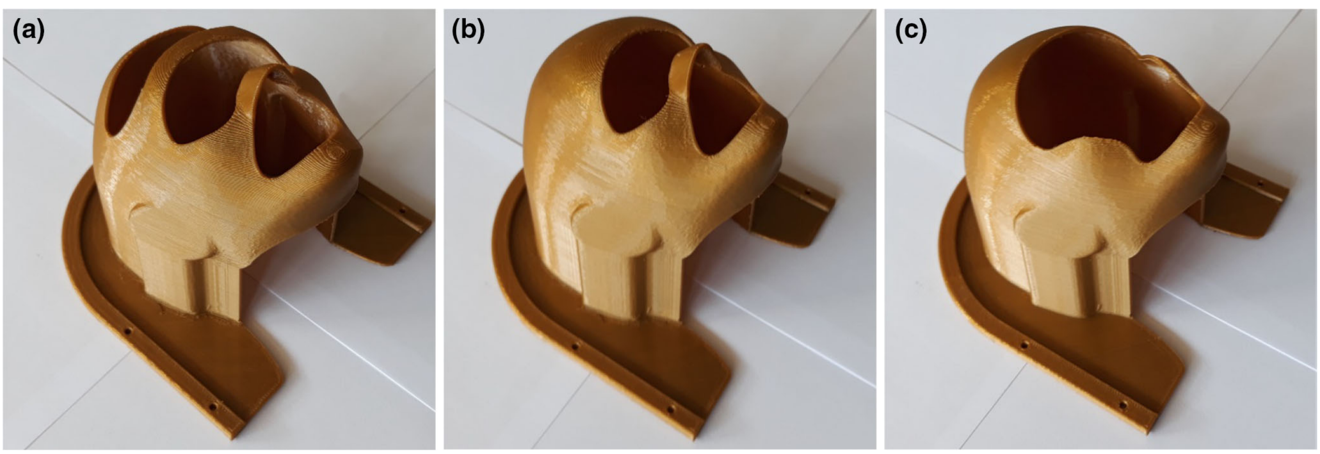

Fig. 15 Mask model M1 (**a**); mask model M2 (**b**); and mask model M3 (**c**)

Table 6 Estimated normalized filament mass and printing time

Infill (%)	M1				M2				M3			
	Hexagonal		Linear		Hexagonal		Linear		Hexagonal		Linear	
	m	Δt	m	Δt	m	Δt	m	Δt	m	Δt	m	Δt
10	0.948	0.963	0.949	0.963	0.962	0.960	0.959	0.960	0.953	0.969	0.949	0.965
20	0.951	0.963	0.954	0.967	0.965	0.963	0.964	0.963	0.955	0.969	0.954	0.969
30	0.955	0.967	0.960	0.973	0.966	0.966	0.964	0.970	0.959	0.973	0.961	0.973
40	0.961	0.973	0.965	0.977	0.969	0.966	0.975	0.966	0.960	0.973	0.963	0.977
50	0.961	0.973	0.971	0.980	0.972	0.970	0.981	0.976	0.964	0.977	0.970	0.980
60	0.969	0.980	0.978	0.987	0.971	0.976	0.979	0.983	0.967	0.980	0.976	0.984
70	0.972	0.983	0.983	0.990	0.974	0.980	0.984	0.983	0.970	0.980	0.981	0.988
80	0.975	0.983	0.988	0.993	0.977	0.983	0.989	0.990	0.973	0.984	0.987	0.992
90	0.978	0.987	0.994	0.997	0.978	0.983	0.994	0.993	0.976	0.984	0.993	0.996
100	1.000	1.000	1.000	1.000	1.000	1.000	1.000	1.000	1.000	1.000	1.000	1.000

procedural modifications will be necessary to enable their future use.

Acknowledgements The authors wish to acknowledge Fundação Champalimaud for the possibility of obtaining the CT images, which were essential to this study.

References

1. J. Ferlay, I. Soerjomataram, M. Ervik, R. Dikshit, S. Eser, C. Mathers, M. Rebelo, D.M. Parkin, D. Forman, F. Bray, GLOBOCAN 2012: estimated cancer incidence, mortality and prevalence worldwide in 2012 v1.0. IARC CancerBase no. 11. ISBN-13 978-92-832-2447-1
2. National Cancer Institute, A Snapshot of Head and Neck Cancer, Institute, U.S. Department of Health and Human Services, 2013 (27 Jan 2015)
3. S. Pelengaris, M. Khan (eds.), *The Molecular Biology of Cancer* (Blackwell and Publishing, Oxford, 2006), pp. 1–30
4. A. Rahmim, K. Dinelle, J.C. Cheng et al., Accurate event-driven motion compensation in high-resolution PET incorporating scattered and random events. IEEE Trans. Med. Imaging **27**(8), 1018–1033 (2008). https://doi.org/10.1109/TMI.2008.917248
5. M. Wardak, K.P. Wong, W. Shao et al., Movement correction method for human brain PET images: application to quantitative analysis of dynamic 18F-FDDNP scans. J. Nucl. Med. **51**(2), 210–218 (2010). https://doi.org/10.2967/jnumed.109.063701
6. J. Mar, M.S. Monteiro, V.F. Vieira et al., Value of a lower limb immobilization device for SPECT/CT image fusion optimization. J. Nucl. Med. Technol. **43**(2), 98–102 (2015). https://doi.org/10.2967/jnmt.114.145771
7. A. Tessitore, A. Giordano, R. De Micco et al., Sensorimotor connectivity in Parkinson's disease: the role of functional neuroimaging. Front. Neurol. **5**, 180 (2014). https://doi.org/10.3389/fneur.2014.00180
8. M. Fisher, C. Applegate, M. Ryalat et al., Evaluation of 3-D printed immobilisation shells for head and neck IMRT. Open J. Radiol. **4**, 322–328 (2014). https://doi.org/10.4236/ojrad.2014.44042
9. S. Chen, Y. Lu, C. Hopfgartner et al., 3-D Printing based production of head and neck mask for radiation therapy using CT volume data: a fully automatic framework, in *Proceeding-International Symposium on Biomedical Imaging* (2016), pp. 403–406. https://doi.org/10.1109/isbi.2016.7493293
10. E. Sousa, L. Vieira, D. Costa et al., Comparison between 3d laser scanning and computed tomography on the modelling of head surface, in *3rd International Conference on Numerical and Symbolic Computation—SYMCOMP 2017. Guimarães, Portugal. ECCOMAS—European Community on Computational Methods in Applied Sciences* (2017), pp. 119–128
11. M.A.R. Loja, E. Sousa, L. Vieira, D.M.S. Costa, D.S. Craveiro, R. Parafita, D.C. Costa, Using 3D anthropometric data for the modelling of customised head immobilisation masks. Comput. Methods Biomech. Biomed. Eng. Imaging Vis. (2019). https://doi.org/10.1080/21681163.2018.1507840
12. J. Schindelin, I. Arganda-Carreras, E. Frise et al., Fiji: an open-source platform for biological-image analysis. Nat. Methods **9**(7), 676–682 (2012). https://doi.org/10.1038/nmeth.2019
13. SolidWorks. https://www.solidworks.com/product/solidworks-simulation. Accessed 10 Jan 2018
14. Material Property Data – MATWEB. 2017. http://www.matweb.com/index.aspx. Accessed 10 Jan 2018
15. Gamma Compatible Materials. 2011. Nordion: Science Advancing Health. http://www.nordion.com. Accessed 27 Dec 2017
16. J.N. Reddy, *An Introduction to the Finite Element Method*, 2nd edn. (McGraw-Hill, New York, 1984)
17. M.A.R. Loja, J.I. Barbosa, C.M. Mota Soares, Analysis of sandwich beam structures using kriging based higher order models. Compos. Struct. **119**, 99–106 (2015). https://doi.org/10.1016/j.compstruct.2014.08.019
18. S. Almosnino, L. Pelland, J.M. Stevenson, Retest reliability of force-time variables of neck muscles under isometric conditions. J. Athl. Train. **45**, 453–458 (2010). https://doi.org/10.4085/1062-6050-45.5.453